# Pinning-depinning transition of fronts between standing waves

Marcel G. Clerc[*] and Cristian Fernández-Oto[†]
*Departamento de Física, Facultad de Ciencias Físicas y Matemáticas, Universidad de Chile, Casilla 487-3, Santiago Chile*

Saliya Coulibaly[‡]
*Laboratoire de Physique des Lasers, Atomes et Molécules, CNRS UMR 8523, Université de Lille 1 Sciences et Technologies, 59655 Villeneuve d'Ascq Cedex, France, EU*

(Received 16 May 2012; published 3 January 2013)

Dynamic behaviors of fronts connecting standing waves, such as the locking phenomenon, pinning-depinning transitions, propagation, and front interactions, are studied. Two systems are considered, a vertically driven pendulum chain and a generalized $\phi^4$ model. Both models exhibit in an appropriate region of parameters bistability between standing waves. In the driven pendulum chain, using a Galerkin expansion we characterize the region of bistability between subharmonic waves for the upright and the upside-down pendulum states. We derive analytically the front dynamics in the generalized $\phi^4$ model, showing regions where fronts are oscillatory or propagative. We also characterize the mechanism of the pinning-depinning transition of fronts between standing waves. Using front interactions we predict the emergence of dissipative localized waves supported on a standing wave and characterize their corresponding homoclinic snaking bifurcation diagrams. All these analytical predictions are confirmed by numerical simulations with quite good agreement.

DOI: 10.1103/PhysRevE.87.012901 PACS number(s): 05.45.−a, 47.20.Ky, 47.54.−r

## I. INTRODUCTION

Nonequilibrium systems—systems with injection and dissipation of energy and momentum—are characterized by their ability to exhibit self-organized structures or patterns [1–3]. Usually, nonequilibrium processes in nature lead to the formation of spatially periodic structures developed from a homogeneous state through the spontaneous breaking of the symmetries which are present in the systems [1]. In the course of recent decades, much effort has been devoted to the study of pattern formation arising in situations such as chemical or catalytic reaction systems, gas discharge systems, nonlinear optics, magnetic media, liquid crystals, hydrodynamics, granular media, and vegetation population, to mention a few (see [4–6] and the references therein). Hence, it is a commonplace to use a unified description to study the dynamics of spatially periodic structures. Indeed, in most of the aforementioned physical systems, spatially periodic structures can be described at the onset of the bifurcation by means of amplitude equations for the critical or marginal modes [1–5]. In general, such a description is valid in the case of weak nonlinearities and for both slow spatial and temporal variation of the base pattern.

Another typical feature of nonequilibrium systems is their capacity to exhibit multistability, leading to the coexistence of different equilibria. Consequently, a disturbance in these systems undergoes an evolution that ends with the formation of different domains separated by *walls*, *fronts*, or *interfaces* [2]. Later, the dynamics of these fronts stems from the attributes of the connected states. For one-dimensional spatially extended systems, the theoretical description of fronts is rather well established. Indeed, in this case, fronts are understood as heteroclinic solutions connecting different equilibrium states [7,8]. From the dynamical point of view, a front that connects two stable uniform states is characterized by the invasion of the more favorable state into the less favorable one at a constant speed [7], which is proportional to the energy difference between these states when the systems are variational [7,9]. Hence, one may expect a front connecting two symmetric states to be stationary or motionless—a *kink solution*. This statement is correct for variational systems, i.e., those where the dynamical evolution minimizes a Lyapunov functional. However, for nonvariational systems by means of a spontaneous breaking of the spatial reflection symmetry, kink solutions can propagate with constant speed [10].

The above scenario changes, when one considers a front connecting a stable pattern with a stable uniform state. The main trait in this case is the emergence of a *pinning range*, i.e., a region in the parameter space where the fronts are motionless [7]. That is, although one state is more favorable than the other, it cannot invade due to a nucleation barrier that results from the coupling of the envelope variations and the underlying pattern [11]. Then, changing the control parameters, one may reach a critical value—*the pinning-depinning transition point*—beyond which a front travels with an oscillatory speed. This propagative behavior is characterized by two regimes: (i) an oscillatory motion of the front characterized by periodic leaps or relaxation oscillations with a large period [12], i.e., the periodic leaps consist of a slow buildup followed by a sudden relaxation, followed by another slow buildup and so forth; and (ii) a harmonic oscillatory motion. These regimes are observed, respectively, for values of the parameters close to and far from the pinning-depinning transition point [13]. Recently, experimental evidence of the dynamical behavior of these type of fronts has been given in Ref. [14]. In the case of fronts connecting one pattern with another, one observes qualitatively the same scenario. This is also a consequence of the coupling between the envelope variations and the underlying pattern,

[*]marcel@dfi.uchile.cl
[†]crfernan@ing.uchile.cl
[‡]saliya.coulibaly@phlam.univ-lille1.fr

 

which induces a nucleation barrier at the interface of the front. However, the above scenario is still incomplete, since the properties of a front between standing waves remain to be characterized. The behavior of these fronts is not obvious, since as a result of the wave spatial period one would expect to observe the pinning phenomenon. On the other hand, the wave oscillations should destroy the nucleation barrier resulting from the coupling between the envelope variations and the underlying pattern. Then, one would expect the dissolution of the locking phenomenon.

The purpose of this paper is to clarify the existence, stability properties, dynamical evolution, and bifurcation diagram of fronts connecting two standing waves in one-dimensional extended systems. To achieve these purposes we consider two examples: a driven vertically pendulum chain and a generalized $\phi^4$ model. Note that both models under consideration are paradigmatic models in nonlinear science. The pendulum chain is the prototype model of energy transport and nonlinear waves [15,16] and the $\phi^4$ model is the prototype equation of spontaneous breaking of symmetry [17]. Both models have regions of parameters where bistability between standing waves can be observed. In the case of the vertically driven pendulum chain, we have characterized analytically the region of bistability between subharmonic waves supported by both upright and inverted pendulum states by means of the Galerkin method. Numerical simulations of the parametrically driven sine-Gordon equation describing the motion of the pendulum chain display a good agreement with the theoretical result. We have also characterized analytically the front dynamics in the generalized $\phi^4$ model, showing regions where fronts are oscillatory or propagative. The pinning-depinning transition mechanism between these standing waves has been singled out with good agreement with numerical simulations. In the two systems under consideration, the interaction of the observed front leads to the emergence of dissipative localized waves. The derivation of the front interaction allows us to describe accurately their respective homoclinic snaking bifurcation diagrams.

The paper is organized as follows: The characterization of the bistability regions and existence of front solutions for a vertically driven pendulum chain is presented in Sec. II. For sufficiently large frequencies and amplitudes the system exhibits coexistence between subharmonic waves for vertical and inverted pendula. In Sec. III, the existence, stability properties, dynamical evolution, and bifurcation diagram of a front connecting two standing waves in the generalized $\phi^4$ model is presented. Based on front interactions, in Sec. IV the existence and the bifurcation diagrams of localized waves are studied. Finally, the conclusions are presented in Sec. V.

## II. FRONT SOLUTION BETWEEN STANDING WAVES IN A VERTICALLY DRIVEN PENDULUM CHAIN

A simple physical system exhibiting standing waves is a vertically driven damped pendulum chain, which is described in the continuum limit by the parametrically driven sine-Gordon equation

$$\ddot{\theta}(z,t) = -\left[\omega_0^2 + \gamma \sin(\omega t)\right] \sin\theta - \mu\dot{\theta} + \kappa\,\partial_{zz}\theta, \qquad (1)$$

where $\theta(z,t)$ is the angle formed by the pendulum and the vertical axis in the $z$ position at time $t$, $\omega_0$ is the pendulum's natural frequency, and $\{\mu,\kappa,\gamma,\omega\}$ are the damping, elastic coupling, amplitude, and frequency of the parametric forcing, respectively. Hence, the terms proportional to $\gamma$ and $\mu$ describe the injection and dissipation of energy, respectively. Let us introduce the parameter $a \equiv \gamma/\omega^2$ which accounts for the displacement of the pendulum pivot in units of the pendulum's natural length. Without forcing and damping ($\gamma = \mu = 0$) the above model is a conservative Hamiltonian system, which presents time-reversal invariance. Hence, the inclusion of injection and dissipation of energy can lead to complex spatiotemporal dynamics which are usually observed in nonequilibrium systems. Notice that Eq. (1) also has the reflection symmetry $\theta \to -\theta$.

A simple homogeneous state of Eq. (1) is $\theta(z,t) = 0$, which stands for a uniform vertical oscillation of pendula. It is well known that when the pendulum chain is forced close to twice the natural frequency—$\omega = 2(\omega_0 + \nu)$, where $\nu \ll 1$ is the detuning parameter—the vertical solution becomes unstable at $\nu^2 + \mu^2/4 = \gamma^2/16$ for small $\{\nu,\gamma,\mu\}$ [18]. In the $\nu\gamma$ space or equivalently $\omega a$ space, this curve is known as the *Arnold tongue* as shown in Fig. 1. In this figure, the solid curve $\Gamma_1$ corresponds to the Arnold tongue for small [Figs. 1(a) and 1(b)] and large dissipation [Fig. 1(c)]. In the limit of small dissipation, one intuitively expects that when the system is forced at $2\omega_0$ the term $\gamma \sin(\omega t)\sin\theta$ oscillates at the natural frequency $\omega_0$ and thus forces the oscillator at its natural frequency. This generates an efficient mechanism of energy injection that is responsible for parametric resonance. Elsewhere, one expects that for any frequency $\omega$ a value of $\gamma$ might exist for which the vertical solution is unstable, because the injection of energy in a period of oscillation is greater than the corresponding energy dissipation. To characterize this parametric resonance curve in the case of a single pendulum ($\kappa = 0$), we use the following expansion as proposed in Ref. [19]: $\theta(t) = A_1 e^{i\omega t/2} + A_3 e^{i3\omega t/2} + \cdots + \text{c.c.}$ (where the symbol c.c. stands for the complex conjugate); introducing this expansion in Eq. (1) with $\kappa = 0$, and linearized in the complex amplitude $A_n$ ($n = 1,3,5,\ldots$), one gets a set of equations for $A_n$ with constant coefficients. The instability curve is derived by means of imposing the requirement that this linear system has a nonzero solution. As shown in Ref. [19] with a small number of the first modes—the *Galerkin method* [20]—one obtains a quite good approximation to the instability curve. For instance, considering the first two modes $\{A_1,A_3\}$, one obtains the marginal curve

$$\begin{aligned}&\frac{9\mu^4\omega^4}{16} + \frac{45\mu^2\omega^6}{32} - \frac{3}{16}a^2\mu^2\omega^6 + \frac{81\omega^8}{256} - \frac{99a^2\omega^8}{64}\\ &\quad + \frac{a^4\omega^8}{16} - \frac{9}{4}\mu^2\omega^4\omega_0^2 - \frac{45\omega^6\omega_0^2}{16} + \frac{19}{8}a^2\omega^6\omega_0^2\\ &\quad + \frac{5}{2}\mu^2\omega^2\omega_0^4 + \frac{59\omega^4\omega_0^4}{8} - \frac{3}{4}a^2\omega^4\omega_0^4 - 5\omega^2\omega_0^6\\ &\quad + \omega_0^8 = 0. \qquad (2)\end{aligned}$$

Figure 1 shows this curve, which is denominated as $\Gamma_1$. Above the $\Gamma_1$ curve the uniform vertical solution is unstable.

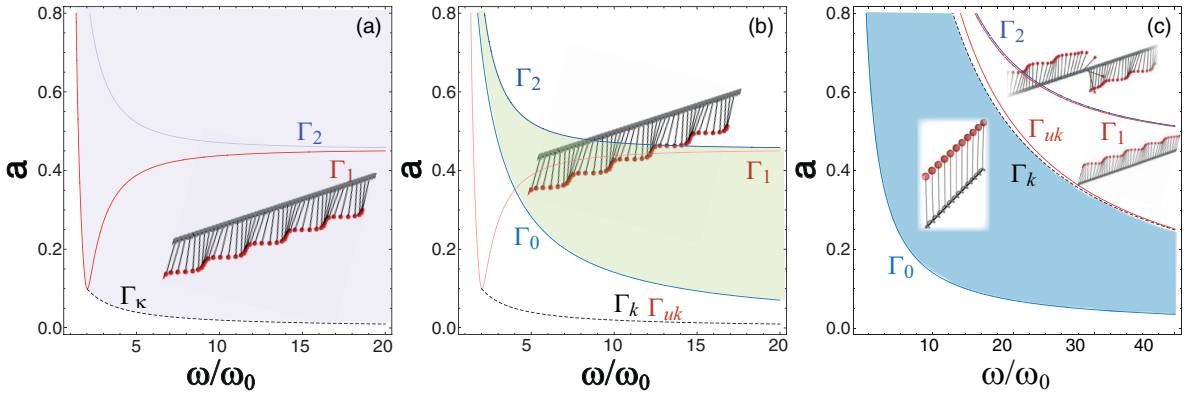


FIG. 1. (Color online) Bifurcation diagram of parametrically driven chain of pendula. (a) Bifurcation diagram for vertical uniform solution $\theta(x,t) = 0$ for small dissipation $\mu = 0.2$. The $\Gamma_k$ and $\Gamma_1$ curves are stationary instabilities with and without space, respectively, of the uniform upright pendulum oscillation. The shaded region shows where standing waves are observed. The inset illustrates the standing wave typically observed. (b) and (c) Bifurcation diagram for upside-down pendula $\theta(x,t) = \pi/2$, for small ($\mu = 0.2$) and large ($\mu = 10$) dissipation, respectively. $\Gamma_0$ and $\Gamma_{uk}$ are, respectively, the curve that accounts for the inverted pendulum stabilization through the Kapitza effect and the spatial instability curve for uniform inverted pendula. Note that in the central panel that corresponds to small dissipation, the $\Gamma_{uk}$ curve has no relevant differences from the $\Gamma_k$ curve. $\Gamma_2$ stands for the stationary instability curve for a single upside-down pendulum. In the shaded regions in (b) and (c) are observed, respectively, a stable single upside-down and a stable uniform upside-down pendulum.

To study the stability of the uniform vertical oscillation ($\kappa \neq 0$), we consider an extension of the previous expansion. Thus, we use the following ansatz:

$$\theta(x,t) \approx A_1 e^{i\omega t/2+ikx+\lambda t} + A_3 e^{i3\omega t/2+ikx+\lambda t} + \text{c.c.} \quad (3)$$

Introducing this ansatz in Eq. (1), linearized in the complex amplitudes, and imposing the requirement that this linear system has a nonzero solution, one finds the expression for the growth rate $\lambda(k)$. The spatial instability curve is derived by requiring that the global maximum of $\lambda(k)$ is zero with $k \neq 0$. We obtain the expression

$$36\mu^3\omega^2 - 36a\mu^2\omega^3 + 81\mu\omega^4 + 12a^2\mu\omega^4 - 81a\omega^5 - 72\mu\omega^2\omega_0^2 + 72a\omega^3\omega_0^2 + 16\mu\omega_0^4 - 16a\omega\omega_0^4 = 0. \quad (4)$$

This curve is represented by the dashed curve $\Gamma_k$ in Fig. 1. Below (above) this curve the uniform oscillation ($\theta = 0$) is stable (unstable). Then the system exhibits a spatial instability giving rise to standing waves with wavelength $k_c^2 = \omega^2/4 - \omega_0^2 - a^2\omega^4(9\omega^2 - 4\omega_0^2)/[(9\omega^2 - 4\omega_0^2)^2 + 36\mu^2\omega^2]$ at frequency $\omega/2$. In the inset of Fig. 1(a) is illustrated the typical pattern observed above the $\Gamma_k$ curve. The shaded region represents the region where standing waves around the uniform upright pendula are observed.

On the other hand, it is well known that a vertically driven pendulum chain at high frequencies can stabilize the inverted pendulum, the *Kapitza effect* [21]. It is important to note that the upside-down state becomes stable at high frequencies even for small displacement of the support point. This counterintuitive fact was first predicted analytically in a simple driven pendulum by the pioneering work of Stephenson [22] which spanned a large amount of theoretical [21,23] and experimental discussions [24,25] of the phenomenon. The stabilization of the inverted state can be understood as a result of time scale separation between the forcing and the state variable $\theta$ itself, producing the appearance of an effective force. Using the strategy proposed by Kapitza [26], which is based on the decomposition of the evolution of $\theta$ into a slow and rapid dynamics, one finds that the vertical solution is stabilized when [21,26]

$$a^2 \geqslant 2\frac{\omega_0^2}{\omega^2}. \quad (5)$$

The shaded region in Fig. 1(c) represents the region where the uniform inverted pendulum state is stable and the curve $a^2 = 2\omega_0^2/\omega^2$ is represented by $\Gamma_0$. To study the stability of an upside-down pendulum, we proceed as for the case of the upright pendulum, with the only difference that in the linear equation for $\theta\omega_0$ should be replaced by $i\omega_0$ and $\kappa = 0$, which changes the sign of the first term of Eq. (1). One obtains the marginal curve [19]

$$\frac{9\mu^4\omega^4}{16} + \frac{45\mu^2\omega^6}{32} - \frac{3}{16}a^2\mu^2\omega^6 + \frac{81\omega^8}{256} - \frac{99a^2\omega^8}{64} + \frac{a^4\omega^8}{16} + \frac{9}{4}\mu^2\omega^4\omega_0^2 + \frac{45\omega^6\omega_0^2}{16} - \frac{19}{8}a^2\omega^6\omega_0^2 + \frac{5}{2}\mu^2\omega^2\omega_0^4 + \frac{59\omega^4\omega_0^4}{8} - \frac{3}{4}a^2\omega^4\omega_0^4 + 5\omega^2\omega_0^6 + \omega_0^8 = 0. \quad (6)$$

This curve is represented by $\Gamma_2$ in Fig. 1. In a similar manner ($\kappa \neq 0$), for the spatial stability of uniform upside-down pendula, we derived the following spatial marginal curve for uniform upright pendula:

$$36\mu^3\omega^2 - 36a\mu^2\omega^3 + 81\mu\omega^4 + 12a^2\mu\omega^4 - 81a\omega^5 + 72\mu\omega^2\omega_0^2 - 72a\omega^3\omega_0^2 + 16\mu\omega_0^4 - 16a\omega\omega_0^4 = 0. \quad (7)$$

This curve is represented by $\Gamma_{uk}$ in Fig. 1. Above this curve we observe that the uniform inverted pendula exhibit a supercritical spatial bifurcation, which gives rise to the emergence of a standing wave with wavelength $k_{c1}^2 = \omega^2/4 + \omega_0^2 - a^2\omega^4(9\omega^2 + 4\omega_0^2)/[(9\omega^2 + 4\omega_0^2)^2 + 36\mu^2\omega^2]$ at the frequency $\omega/2$. It is important to note that the difference between the curves $\Gamma_{uk}$ and $\Gamma_k$ are noticeable only for large

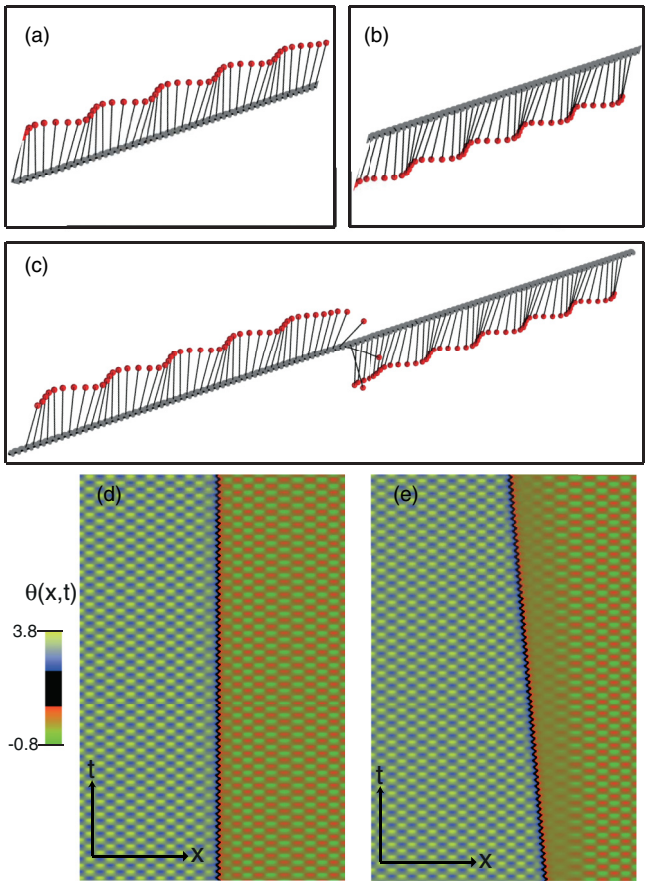


FIG. 2. (Color online) Front solution connecting standing waves in a vertically driven pendulum chain: (a) standing wave of vertical pendula, (b) standing wave of upside-down pendula, and (c) front solution connecting these states obtained from model (1), with $\omega_0 = 0.01$, $\gamma = 1.17$, $\omega = 1.0$, $\mu = 1.0$, and $\kappa = 1.0$. Spatiotemporal diagram of the front solution connecting vertical and inverted pendulum waves obtained from model (1), with $\gamma = 1.7$, $\mu = 1.0$, $\omega = 1.0$, $\kappa = 1.0$, and (d) $\omega_0 = 0.001$ and (e) $\omega_0 = 0.2$. The values on the axes are given in arbitrary units.

dissipation (see Fig. 1). The $\Gamma_{uk}$ curve may be below or above the Kapitza curve $\Gamma_0$ depending on whether the dissipation is large or small, respectively. Therefore, one would not expect to observe standing waves around the upside-down state for small dissipation because the spatial instability anticipates stabilization for high frequencies [see Fig. 1(b)]. Conversely, for large dissipation one expects to see a region of parameters where the upside-down state and the standing waves around the inverted pendulum are stable [see Fig. 1(c)].

It is worthy of note that for large dissipation in the region above the $\Gamma_2$ curve, the vertically driven pendulum chain displays a coexistence between standing waves destabilizing the upright and upside-down states. Hence, one can find solutions which connect these two standing waves—the *front solution*. Figures 1 and 2 show the standing wave solution of vertical, inverted pendula, and the front solution connecting these states for the same parameters. As a result of gravity the vertical pendulum wave is always more stable than the inverted one. Thus one expects that the front propagates such that the vertical pendulum wave invades inverted pendulum waves. Figure 2(e) shows the propagation of this front through the spatiotemporal diagram of the field $\theta$. Surprisingly, when one modifies the parameters, the front becomes motionless although the vertical pendulum wave is more stable—this is the *locking phenomenon*. This behavior is observed in a wide region of parameters. The spatiotemporal diagram of Fig. 2(d) shows a motionless front.

From these numerical observations arises the query as to what is the mechanism that causes the locking of the front propagation—the *pinning effect*. Due to the lack of analytical expressions for the waves of upside-down and upright pendula, and their respective fronts, it is troublesome to understand the front dynamics and the mechanism that generates the locking phenomenon. Thus for the sake of simplicity, we shall consider a simpler model that allows us to infer analytically the front dynamics and then verify these properties in the vertically driven pendulum chain.

## III. SIMPLIFIED MODEL FOR A FRONT CONNECTING STANDING WAVES

Let us consider the following generalized $\phi^4$ model:

$$\partial_{tt}u = \eta + u - u^3 + \partial_{xx}u + \mu\partial_t u + \nu \sin(kx)\cos(\omega t). \tag{8}$$

Note that for $\eta = \mu = \nu = 0$ the above equation is the well-known $\phi^4$ model [17]. This model is characterized by having two stable symmetric uniform states $u = \pm 1$ and front solutions that connect these states, which are usually called *kink solutions*. Figure 3(a) shows a kink solution of Eq. (8). For the generalized $\phi^4$ model $\mu$ is the damping parameter which accounts for the energy dissipation and $\eta$ is a parameter that breaks the reflection symmetry of this model. In that sense this parameter plays a similar role to gravity in a vertically driven pendulum chain. For $\eta \neq 0$, the more favorable state invades the less favorable one, and then the front propagates ($\nu = 0$). For small $\eta$, it is easy to show that the speed is proportional to $\eta$ [7]. Then, for $\eta = 0$ the system has a Maxwell point [27], i.e., both uniform states are energetically equivalent. The parameter $\nu$ measures the strength of the spatiotemporal forcing, which causes the uniform states to become standing waves with amplitudes proportional to $\nu$. Figure 3(b) shows how the fronts are modified in the presence of spatiotemporal forcing and the spatiotemporal diagrams Figs. 3(c) and 3(d) illustrate the front dynamics of the standing waves. Numerically, we observe that for $\eta \neq 0$ the front is motionless in a wide region of parameters [see Fig. 3(c)] and when one increases $\eta$ from a critical value the fronts become propagative [see Fig. 3(d)]. Note that this is a similar dynamic to that observed in the parametrically driven pendulum chain at high forcing frequencies and amplitudes.

### A. Analytical description of the front dynamics

For $\nu = \eta = 0$, the kink solution of model (8) may be written as

$$u_k(x,x_k) = \tanh\left[\frac{x - x_k}{\sqrt{2}}\right], \tag{9}$$

where $x_k$ is a continuous parameter that parametrizes the family of kink solutions, which is a consequence of the

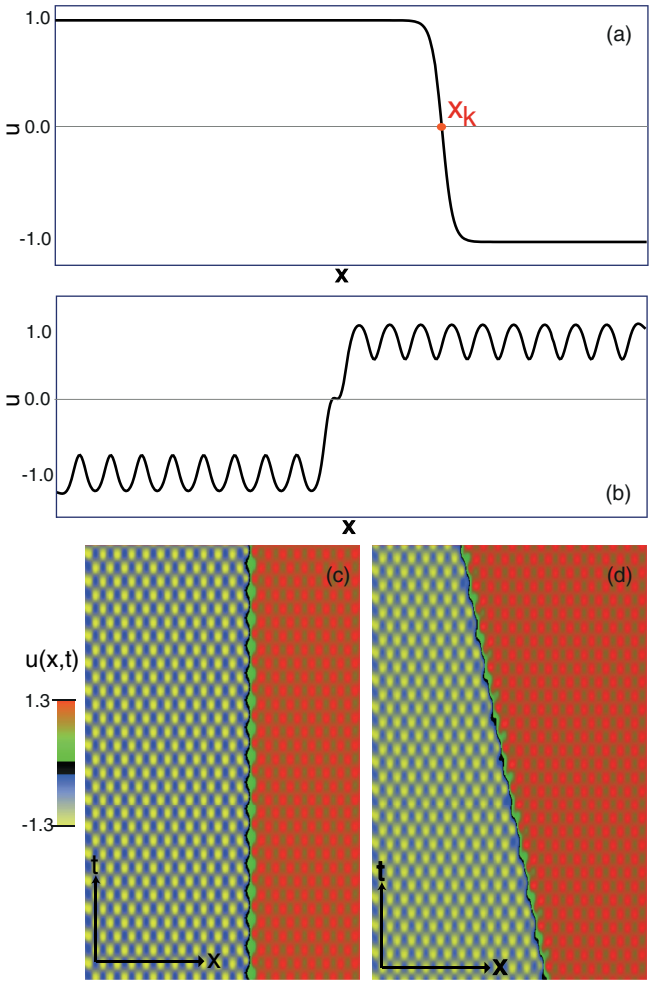


FIG. 3. (Color online) Front solution of generalized $\phi^4$ model (8). (a) Kink solution obtained for by $\eta = 0.0$, $\mu = 0.5$, $k = 1.0$, $\omega = 1.0$, and $\nu = 0.0$. (b) Front solution obtained for by $\eta = 0.001$, $\omega = 1.0$, $\mu = 1.0$, and $\nu = 0.6$. Spatiotemporal diagram of front solution connecting standing waves obtained from model (8), for $\omega = 1.0$, $\mu = 1.0$, $k = 1.0$, $\nu = 0.6$, and (c) $\eta = 0.001$ and (d) $\eta = 0.14$. The values on the axes are given in arbitrary units.

spatial translation invariance of model (8). $x_k$ represents the point where the derivative of the kink solution has its global maximum [see Fig. 3(a)], usually denominated the *core of the front*. Because of the reflection symmetry of the $\phi^4$ model, the system has antikink solutions $u_{ak}(x,x_k) = -u_k(x,x_k)$. If $\nu$, $\mu$, and $\eta$ are small (perturbative terms), then one can consider the following ansatz for the kink solution:

$$u(x,t) = u_k[x - x_k(t)] + W(u_0,x_k,x,t), \tag{10}$$

where $x_k(t)$ has been promoted to a temporal function and $W$ is a small correction function. In what follows we also assume that these functions have a slow temporal variation, i.e., $W \ll 1$, $\partial_t W \ll 1$, and $\partial_t x_0 \ll 1$. Introducing the above ansatz in Eq. (8) and linearizing in $W$, we obtain at the leading order

$$-\mathcal{L}W = \partial_x u_k(\mu\partial_t x_0 + \partial_{tt} x_0) + \eta + \nu \sin(kx)\cos(\omega t), \tag{11}$$

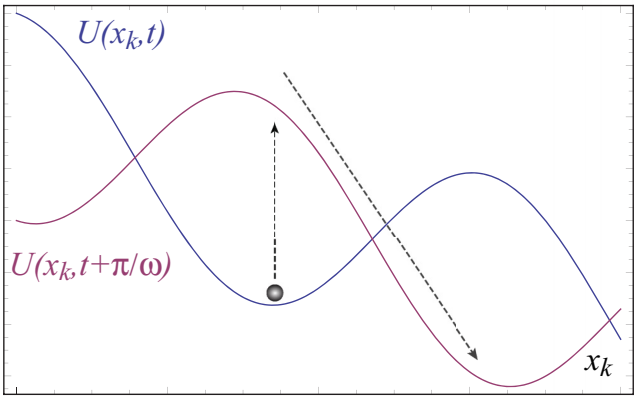


FIG. 4. (Color online) Schematic representation of the mechanism of the front core propagation. The curves account for the core of the front potential a given time $U(x_k,t)$ and a half period later $U(x_k,t+\pi/\omega)$.

where $\mathcal{L} \equiv 1 - 3u_k^2 + \partial_{xx}$ is a linear operator of the Sturm-Liouville type [28]. Introducing the inner product

$$\langle f|g\rangle \equiv \int_{-\infty}^{\infty} f(x)g(x)dx, \tag{12}$$

the above linear operator becomes self-adjoint. To solve Eq. (11), we use the solvability condition or Fredholm alternative [2]. That is, we multiply by $\partial_x u_k$ and integrate in the whole space of Eq. (11). After straightforward calculations based on residue integration, we obtain

$$\begin{aligned}\ddot{x}_k &= -\mu\dot{x}_k - \frac{3\eta}{\sqrt{2}} - \frac{3\pi k\nu\cos(\omega t)}{2\sinh(\pi k/\sqrt{2})}\sin(kx_k)\\ &= -\mu\dot{x}_k - \frac{\partial U}{\partial x_k},\end{aligned} \tag{13}$$

where the core of the front potential has the form

$$U(x_k,t) = \frac{3\eta}{\sqrt{2}}x_k - \frac{3\pi\nu\cos(\omega t)}{2\sinh(\pi k/\sqrt{2})}\cos(kx_k), \tag{14}$$

which is a temporal $2\pi/\omega$-periodic function. Therefore, the core of the front satisfies a Newton-type equation. This equation is characterized by a damping constant and periodic force with an oscillatory amplitude. The derivation of analytical solutions of model (13) is a thorny task. Intuitively, for $\eta \neq 0$ and small $\nu$, one expects the front core to propagate. Indeed, if at the beginning of a period $x_k$ is located in a minimum of the potential (see Fig. 4), at half the period it will be located close to the maximum, and then it will move toward the nearest global potential minimum in order to minimize the energy (see Fig. 4). Hence, $x_k$ propagates toward a given direction determined by the sign of $\eta$.

The above mechanism of propagation can be interrupted in the case that the forcing $\nu$ is large enough, since the core of the front fails to move to the next minimum, leading to oscillation of the core of the front around a given equilibrium position—the *pinning phenomenon*.

### B. Front dynamics at high frequency and large amplitude

In the case of large frequency and forcing amplitude with respect to the characteristic dynamics of the unforcing system

($\nu = 0$), we can use the Kapitza method to obtain an effective dynamic for Eq. (13). Consequently, the dynamics of the core of the front can be decomposed into a rapid and a slow evolution, that is,

$$x_k(t) = z(t) + y(t), \tag{15}$$

where the rapid dynamics $y(t)$ is small ($y \ll z$ and $1 \ll \dot{y} \ll \ddot{y}$). Using the above ansatz in Eq. (13) and linearizing in the fast variable $y$, we get

$$\ddot{z} + \ddot{y} \approx -\mu\dot{z} - \mu\dot{y} - \frac{\partial U(z,t)}{\partial z} - \frac{\partial^2 U}{\partial z^2} y. \tag{16}$$

Hence, when we assume $\omega \gg \mu$ the leading term of the above equation takes the form

$$\partial_{tt} y = -\frac{3\pi k \nu \sin(kz)}{2\sinh(\pi k/\sqrt{2})} \cos(\omega t). \tag{17}$$

Integrating in the rapid scale, we obtain $y(t) = 3\pi k\nu \sin(kz)\cos(\omega t)/2\omega^2 \sinh(\pi k/\sqrt{2})$. Next, considering the average of $x_k$ in a period $2\pi/\omega$ and using the Laplace integral method [29], one obtains

$$\langle x_k \rangle = \frac{\omega}{2\pi} \int_t^{t+2\pi/\omega} x_k dt \approx z(t). \tag{18}$$

Therefore, $z$ and $y$ describe the mean dynamics and the oscillations around it, respectively. Replacing the expression for $y(t)$ in Eq. (16) and averaging over a period $2\pi/\omega$, this equation reads

$$\ddot{z} = -\mu\dot{z} - \frac{3\eta}{\sqrt{2}} - \frac{9\pi^2 k^3 \nu^2}{16\omega^2 \sinh^2(\pi k/\sqrt{2})} \sin(2kz). \tag{19}$$

Consequently, the mean variable also satisfies a Newton-type equation, with the same damping and constant force as in Eq. (13). However, the periodic force with oscillatory amplitude becomes a periodic force with half the spatial period for the mean variable $z$. As a result of the rapid oscillations—high-frequency limit—the effective potential for the core of the front has one-half the spatial period (cf. Fig. 4).

The locking phenomenon, the pinning range, and the pinning-depinning transition of model (8) are easy to understand from Eq. (19); the locking phenomenon is obtained when the mean variable of the core of the front $z(t)$ has stable equilibria. These equilibria correspond to different stable positions of the fronts. On the other hand, the pinning range and the pinning-depinning transition are, respectively, the region of parameters where model (19) has equilibrium points and the bifurcation point of these equilibria. Let us introduce the parameter

$$\Delta \equiv \frac{8\sqrt{2}\eta\omega^2 \sinh^2(\pi k/\sqrt{2})}{3\pi^2 k^3 \nu^2}, \tag{20}$$

which accounts for the ratio between the coefficients of the constant and the periodic forcing of model (19). Introducing $\Delta$ in Eq. (19) we have

$$\ddot{z} = -\mu\dot{z} - \frac{3\eta}{\sqrt{2}\Delta} [\Delta - \sin(2kz)]. \tag{21}$$

Notice that $\Delta$ is proportional to $\eta$; thus to change $\Delta$ is equivalent to modifying $\eta$. Therefore all the analysis below corresponding to increasing $\Delta$ is equivalent to increasing $\eta$. If $\Delta < 0$ and $|\Delta| > 1$, the model (19) does not have equilibria. Then, one infers that the core of the front moves backward and its acceleration increases and decreases periodically; hence the upper state ($u \approx 1$) invades the lower one ($u \approx -1$) with an oscillatory speed. Figure 3(d) shows the corresponding spatiotemporal evolution of the front in this region of parameters. On increasing $\Delta$ ($\eta$), the system exhibits a simultaneous infinite number of saddle-node bifurcations for $\Delta = \Delta_- \equiv -1$. For $\Delta > \Delta_-$ and $|\Delta| < 1$, the system has an infinite number of stable equilibria. Each equilibrium point represents an oscillatory front around a fixed position [see Fig. 3(c)]. On increasing $\Delta$ further, all critical points disappear simultaneously through a saddle node when $\Delta > 0$ and $\Delta = \Delta_+ \equiv 1$. For $\Delta > \Delta_+$ the front core moves forward; hence the lower state invades the upper state with an oscillatory speed. Figure 5(a) shows the average speed of model (8) as a function of $\eta$, which illustrates the above scenario. Note that a front connecting a uniform state with a pattern has the same bifurcation diagram [7,11,14].

For $\Delta_- < \Delta < \Delta_+$ (pinning range) the system exhibits the locking phenomenon and the pinning-depinning transition takes place at $|\Delta| = 1$. From this condition, we found the

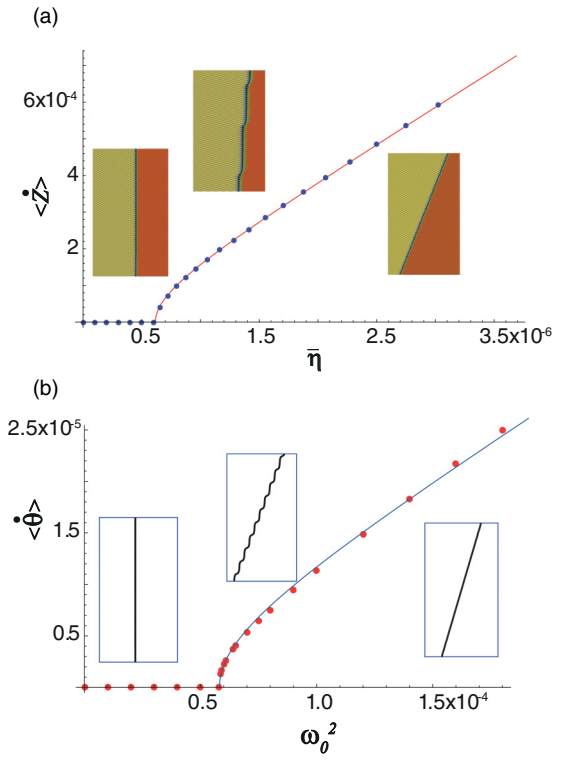


FIG. 5. (Color online) Bifurcation diagram of the front connecting standing waves. (a) Average speed as a function of $\bar{\eta} \equiv 3\eta/\sqrt{2}$ for model (8) with $\omega = 0.05$, $\mu = 0.005$, $k = 2.0$, and $\nu = 0.000\,25$. The circles stand for the values obtained by numerically integrating the model (13) and the solid curve is obtained using formula (23). (b) Average speed as a function of $\omega_0$ for the vertically driven pendulum chain model (1) with $\omega = 4.0$, $\mu = 3.5$, and $\gamma = 15.76$. The circles stand for the values obtained by numerically integrating the model (1) and the solid curve is obtained using formula (23) as a fitting function. The spatiotemporal diagrams inset with time running up depict the front dynamics in the different regions. The values on the axes are given in arbitrary units.

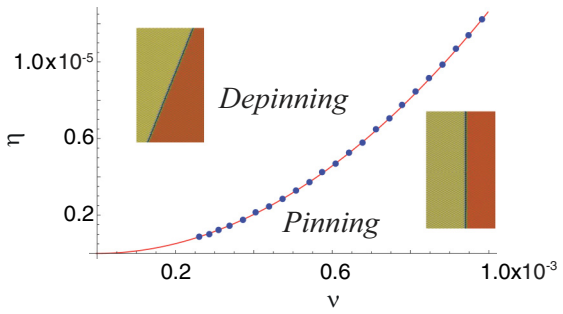


FIG. 6. (Color online) Pinning-depinning transition curve. The solid curve is obtaining using formula (22) with the + sign and the circles stand for the values obtained numerically by integrating model (8) with $\mu = 0.01$, $\omega = 0.1$, and $k = 1.0$. The spatiotemporal diagrams inset with time running up represent, respectively, the typical observed dynamics. The values on the axes are given in arbitrary units.

pinning-depinning transition relation

$$\eta = \pm \frac{3\pi^2 k^3}{8\sqrt{2}\omega^2 \sinh^2(\pi k/\sqrt{2})} \nu^2, \tag{22}$$

which corresponds to a parabolic curve between $\eta$ and $\nu$. Figure 6 shows this pinning-depinning transition curve contrasted with the numerical results obtained from model (8). Notice that the above theoretical prediction has a quite good agreement with the numerical observations. It is important to note that in the $\{\eta, \nu\}$ space the pinning region exhibits a cusp. One can infer that this behavior is a consequence of the cusp catastrophe of the bistability region [30], where the pinning region is circumscribed.

As we have mentioned before, front propagation is characterized by an oscillatory behavior of the speed. In the overdamping limit of model (19), after straightforward calculations one can compute analytically the average speed [13,14]:

$$\begin{aligned} \langle \dot{z} \rangle &= \sqrt{\Delta^2 - 1} \\ &= \sqrt{\left( \frac{8\sqrt{2}\eta\omega^2 \sinh^2(\pi k/\sqrt{2})}{3\pi^2 k^3 \nu^2} \right)^2 - 1}. \end{aligned} \tag{23}$$

Therefore, for $|\Delta| < 1$ the average speed is zero, $\Delta \gtrsim 1$ grows with a square root law, and $\Delta \gg 1$ increases accompanied by a linear law. In Fig. 5(a), the solid curve is obtained using the above formula (23). This curve has a quite good agreement with the numerical observations as shown in Fig. 5(a). The spatiotemporal diagrams inset with time running up depict the front dynamics in the different regions. It is worthy of note that for a front connecting a pattern with a uniform state or pattern state, one can obtain a similar formula for the average front speed [13,14].

The dynamics of the front core is composed of a slow and a rapid dynamics. The slow dynamics describes the average behavior of the front core and the rapid dynamics accounts for the oscillations with respect to the main dynamics. Hence, in the pinning range the front core dynamics is characterized by oscillation around the fixed position. The left-hand side inset in Fig. 5(a) depicts this oscillatory dynamics [see also Fig. 3(c)].

The simplified model (8) exhibits a front connecting two standing waves. These front solutions present the locking phenomenon in a broad region of parameters. Using an adequate limit, we have characterized analytically the coupling between envelope variations and the underlying waves. This is manifested in the equation of the front core [cf. Eqs. (13) and (19)]. Hence, this simplified model allows elucidation of the mechanism of front dynamics that is summarized in Eq. (23). So we have also applied this formula (23) to characterize the front dynamics in a vertically driven pendulum chain. Figure 5(b) shows the average speed of the front connecting standing waves for the vertically driven pendulum chain as a function of the gravity. The circles stand for the values obtained by numerical integration of model (1) and the solid curve is obtained using formula (23) as the fitting function. As can be seen from this figure, we have good agreement between the two results. Hence, we have recognized two different regimes for a front connecting standing waves in a vertically driven pendulum chain: the locking and the propagation regions. This last region is initially characterized by front propagation with periodic leaps or relaxation oscillations [12] that are distinctive for saddle-node bifurcations, and later by front propagation with periodic oscillations.

## IV. LOCALIZED STATES

Localized states arise in dissipative and spatially extended systems and can be seen as patterns extended over a restricted spatial domain, which represents a singleunit or multicellular units. They are characterized by a family of continuous parameters such as the position, the amplitude, and the width. Formally, localized states can be described as particlelike objects, even though made of a large number of fundamental constituents—atoms or molecules. The autocatalytic reaction-diffusion model with inhomogeneous coefficients is one of the pioneering physical contexts where localized states were proposed [31] (for details, see Chap. 7 of Ref. [1] and references therein). Their universal nature has been demonstrated by observation in many fields of physics, with examples including magnetic materials, liquid crystals, gas discharge systems, chemical reactions, fluids, granular media, nonlinear optics, and Bose-Einstein condensates, to mention a few (see the reviews [32–35], and references therein). Many experimental and theoretical works have been devoted to the study of localized structures. Different mechanisms leading to stable localization have been proposed [36]. Among these, two main classes of localized structures have to be distinguished, namely, those localized structures arising as solutions of a quintic Swift-Hohenberg-like equation [37] and those that are stabilized by nonvariational terms in the subcritical Ginzburg-Landau equation [38]. The main difference between the two cases is that the localized structures arising in the first model have a characteristic size which is fixed by the pinning mechanism over the underlying pattern or by spatially damped oscillations between homogenous states [36], whereas the localized structures arising in the second model have no intrinsic spatial length, their size being selected by nonvariational effects and going to infinity when the dissipation goes to zero. Additionally, intriguing dynamical behaviors, displaying mutual interaction of localized structures, have been reported and control methods have been developed in view of potential applications, these mainly aimed at using single-cell

localized structures as elementary, erasable, and rewritable storage bits [39].

The dynamics of localized structures based on pinning mechanisms and the interaction between them have inspired many theoretical works. Most of them are based on a one-dimensional geometrical description, in which localized structures are understood as the homoclinic orbits in the Poincaré section of the corresponding spatially reversible dynamical system [40–43]. In this framework, localized structures are predicted to exist in regions of parameters where the system exhibits bistability between a pattern and a uniform stable state. Localized spatial states are, thus, understood as macroscopic particlelike objects realizing the spatial connection between two metastable states and appearing— the *homoclinic curve*—close to the *pinning range* of the front solution [7]. Inside the pinning range, the bifurcation diagram displays a *snaking* shape with an infinite sequence of saddle-node bifurcations, each bifurcation creating a cell of the localized pattern solution [42]. Extensions of the same scenario have been given in later papers [40,44,45]. More recently, localized structures have been described in terms of front interactions [46] and their existence has been generalized to the case when the homoclinic orbits connect two pattern states, thus leading to *localized peaks* [47].

Close to the pinning range, the vertically driven pendulum chain (1) as well as the simplified model (8) exhibit a family of localized structures with different widths. The widths of the localized structures are roughly multiples of that of the half wavelength of standing waves. Figure 7 shows the typical localized structure and the respective spatiotemporal evolution observed in the vertically driven pendulum chain model (1) and the simplified model (8).

To understand the existence, stability properties, dynamical evolution, and bifurcation diagram of the localized waves, we describe these localized structures as a bound state composed of two fronts [36,46]. Therefore the characterization of the front interactions is a master key to understanding the localized states. For the sake of simplicity, we study the front interactions of model (8) in the limit of small $\eta$ and $\nu$. Since in this limit the fronts interaction is analytically accessible. Thus, a localized structure can be approached by Refs. [36,46]

$$u(x,t) = u_k[x+\delta(t)] + u_{ak}[x-\delta(t)] - 1 + W(x,\delta\delta(t)), \tag{24}$$

where $\{u_k(x),u_{ak}(x)\}$ are, respectively, the kink and the antikink solutions of model (8), $2\delta(t)$ stands for the distance between fronts (see insets in Fig. 8), which is assumed to be larger than the characteristic length of the front ($\delta \gg \sqrt{2}$), and $W$ is a small correction function. Introducing the above ansatz in Eq. (8), using the fact that $u_k(x+\delta)$, $u_{ak}(x-\delta)$, and $u=1$ are solutions of model (8) for $\eta=\nu=0$ and linearizing in $W$, we obtain at dominant order

$$\begin{aligned} &-[1-3(u_k+(u_{ak}-1)]^2+\partial_{xx})W \\ &\quad = -\partial_x u_k(\mu\partial_t\delta+\partial_{tt}\delta)+\partial_x u_{ak}(\mu\partial_t\delta+\partial_{tt}\delta) \\ &\qquad +\left(1-3u_k^2+\partial_{xx}\right)(u_{ak}-1)-3u_k(u_{ak}-1)^2 \\ &\qquad -(u_{ak}-1)^3+\eta+\nu\sin(kx+\phi)\cos(\omega t). \end{aligned} \tag{25}$$

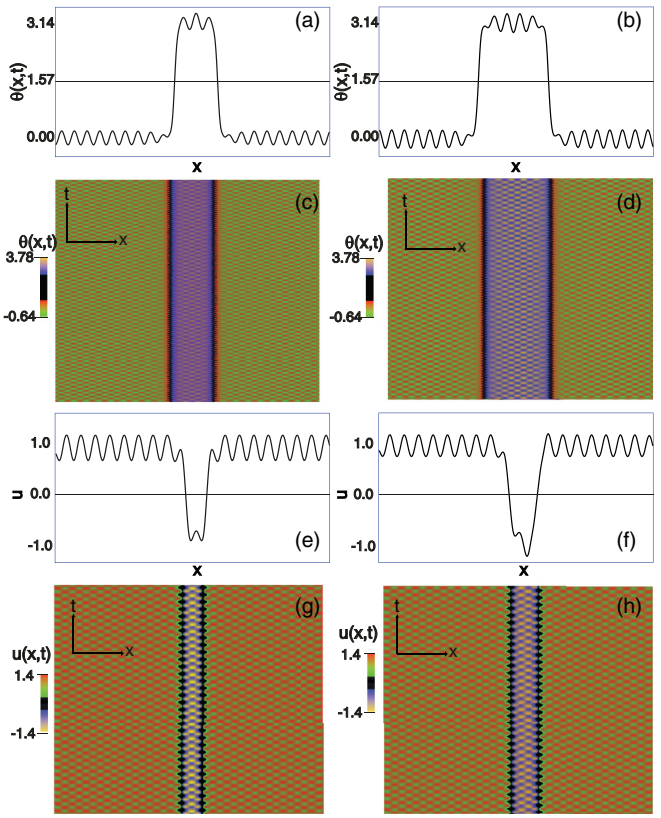


FIG. 7. (Color online) Localized waves. (a), (b), (c), and (d) are profiles and spatiotemporal diagrams of localized waves, respectively, obtained from model (1), with $a=0.83$, $\omega=4.0$, $\mu=3.0$, and $\omega_0^2=0.0001$. (e), (f), (g), and (h) are profiles and spatiotemporal diagrams of localized waves, respectively, obtained from model (8), with $\eta=0.001$, $\omega=1.0$, $\mu=1.0$, $k=1.0$, and $\nu=0.6$. The values on the axes are given in arbitrary units.

Introducing the inner product (12), the linear operator $\mathrm{L} \equiv -[1-3(u_k+(u_{ak}-1)]^2+\partial_{xx})$ is self-adjoint. To solve the above linear equation, we use the solvability condition or

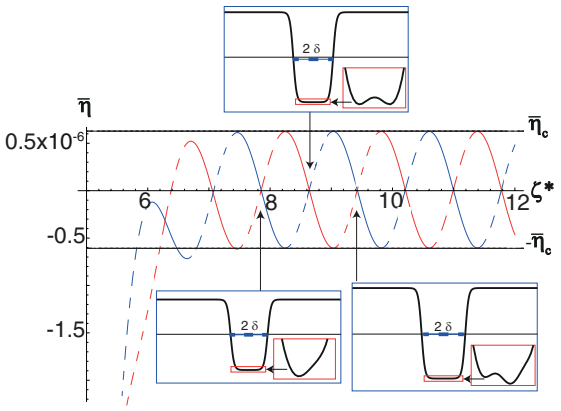


FIG. 8. (Color online) Homoclinic snaking bifurcation diagram of localized waves of model (8) with $k=2$, $\nu=0.000\,25$, and $\omega=0.05$. $\zeta_e$ is the half-width of the localized waves and $\bar{\eta}\equiv 3\eta/\sqrt{2}$. The solid (dashed) lines represent the stable (unstable) localized waves, which were obtained from Eq. (28). The circles account for the numerical equilibrium widths of localized states. The values on the axes are given in arbitrary units.

Fredholm alternative [2], in a similar manner to that used to derive the front core equation (13). After straightforward calculations we obtain

$$\begin{aligned}&\langle \partial_x u_k | \partial_x u_k \rangle \left(\mu \partial_t \delta + \partial_{tt} \delta\right) \\ &\quad = \langle \partial_x u_k | - 3u_k (u_{ak} - 1)^2 - (u_{ak} - 1)^3 \rangle \\ &\qquad + \langle \partial_x u_k | \partial_x u_k \rangle \left( \frac{3\eta}{\sqrt{2}} - \gamma \sin\left[ k\delta + \frac{\phi}{2} \right] \cos(\omega t) \right),\end{aligned} \tag{26}$$

where $\phi$ can be 0 or $\pi$ as a consequence of the discrete translational symmetry and $\gamma \equiv 3\pi k \nu / 2 \sinh(\pi k/\sqrt{2})$. Using the kink and antikink solutions [Eq. (9)], the above equation explicitly reads

$$\begin{aligned}\ddot{\delta} = &-\mu\dot{\delta} - 12e^{-2\sqrt{2}\delta} + \frac{3\eta}{\sqrt{2}} \\ &- \frac{3\pi k \nu}{2\sinh(\pi k/\sqrt{2})} \sin\left( k\delta + \frac{\phi}{2} \right) \cos(\omega t).\end{aligned} \tag{27}$$

Notice that the dynamics between the fronts also satisfies a Newton-type equation, with the additional term $-12e^{-2\sqrt{2}\delta}$, which accounts for the effect of one front on the other one. Therefore, a front exponentially affects the dynamics of the other through this attractive force.

Although Eq. (27) is of Newton type, this is still a complex model to solve analytically. In order to derive analytical expressions we consider a similar procedure as we have done for the front dynamics (Kapitza strategy). Therefore, we may consider the high-frequency and high-amplitude limit. In this limit we obtain the following equation for the mean variable:

$$\ddot{\zeta} - \mu\dot{\zeta} = f(\zeta), \tag{28}$$

where

$$\begin{aligned}f(\zeta) &\equiv -12e^{-2\sqrt{2}\zeta} + \frac{3\eta}{\sqrt{2}} - \frac{9\pi^2 k^3 \nu^2 \sin(2k\zeta + \phi)}{16\omega^2 \sinh^2(\pi k/\sqrt{2})}, \\ \zeta(t) &\equiv \frac{\omega}{2\pi} \int_t^{t+2\pi/\omega} \delta(t) dt.\end{aligned}$$

$f(\zeta)$ describes the effective force in the Newton-type Eq. (28). The equilibria of this system satisfy $f(\zeta^*) = 0$, where $\zeta^*$ accounts for the respective width of the localized structure. Figure 8 shows the equilibria as a function of $\bar{\eta} \equiv 3\eta/\sqrt{2}$, deduced from the above force [Eq. (28)].

From the force $f(\zeta)$ we conclude that for large $\eta$, Eq. (28) like Eqs. (8) and (27), has no bound states, while for small $\eta$ there are bound states. More precisely, for sufficiently large and negative $\eta$, the fronts move away from each other ($\zeta$ increases as a function of time); then the higher standing wave invades the system. When $\eta$ increases ($\eta < 0$), a series of successive saddle-node bifurcations occurs for $\eta \approx -3\pi^2 k^3 \nu^2 / 8\sqrt{2}\omega^2 \sinh^2(\pi k/\sqrt{2})$. These bifurcations generate the appearance of localized structures in pairs, one stable and the other unstable, and each time with a smaller number of bumps. That is, this sequence of bifurcations is characterized by localized states with large widths appearing first and later the states with small ones. These infinite number of bifurcations occur in an exponentially small region as shown in Fig. 8. A similar scenario is observed in the case of localized patterns [40,42].

For small $\eta$, and close to the Maxwell point ($\eta = 0$), the system has an infinite number of localized waves with all the possible number of bumps. The widths of the localized wave are roughly multiples of that of the shortest localized state. In contrast, for $\eta \approx \bar{\eta}_c \equiv 3\pi^2 k^3 \nu^2 / 8\sqrt{2}\omega^2 \sinh^2(\pi k/\sqrt{2})$. The dashed horizontal lines in Fig. 8 illustrate this critical value. The localized waves disappear via saddle-node bifurcations. On increasing $\eta$ the larger localized patterns disappear sequentially one after the other. Hence, the shortest localized state is the last to disappear (see Fig. 8). Thus for sufficiently large and positive $\eta$, fronts attract each other ($\zeta$ decreases as a function of time), and then the lower standing wave invades the system. The same complex structure of bifurcation is observed in localized patterns [40,42]. The above complex scenario is known as the homoclinic snaking bifurcation diagram [42]. Recently, this dynamics has been reported in an experimental work [48].

## V. CONCLUSION

In past decades a great effort has been devoted to understanding the existence, stability properties, dynamical evolution, and bifurcation diagram of localized states in systems out of equilibrium. A simple way to understand these localized states is by considering that they are composed of a bound state of two fronts. Hence, in this framework localized states must be observed in a bistability region. Indeed, in such a region one can observe fronts between the respective states. The dynamical properties of these fronts allow one to understand the corresponding features of the localized structures. In the present work, we have characterized the possibility of fronts and dissipative localized states in systems that exhibit bistability between standing waves. More precisely, we have characterized the locking phenomenon, the pinning-depinning transition, the propagation, and the interaction of this type of front. We have considered two systems: a vertically driven pendulum chain and a generalized $\phi^4$ model. Both systems exhibit in some regions of parameter bistability between standing waves. In the case of the parametrically driven pendulum chain, we have characterized the region of bistability between subharmonic waves for upright and upside-down pendula by using the Galerkin method, obtaining a good agreement between the theoretical and numerical results. The fronts exhibit a rich dynamics, which has been characterized analytically in the generalized $\phi^4$ model, showing the regions where the front is oscillatory and propagative. These results are verified numerically for the vertically driven pendulum chain and the generalized $\phi^4$ model. The analytical characterization of the fronts interaction allows us to predict the emergence of dissipative localized waves and the derivation of their respective homoclinic snaking bifurcation diagrams. Although we have considered two specific paradigmatic examples, it is important to note that the phenomenon under study is universal and that both examples contain the ingredients necessary to observe localized waves and pinning-depinning transitions of the standing waves.

Parametrically driven systems generically exhibit standing waves, Faraday waves; however, they do not necessarily

coexist with other standing waves. One possible strategy to induce coexistence of standing waves is by consider the effects of high frequencies, which can stabilize unstable states and induce their respective *self-parametric resonances* [23]. The results found in this work are general and we expect the effects to be observed in other physical systems exhibiting bistability of standing waves, such as fluids submitted to parametric forcing and forced magnetic systems. Work in this direction is in progress.

**ACKNOWLEDGMENTS**

The authors thanks R. A. Kraenkel and C. Falcón for fruitful discussions. The authors acknowledge financial support by ANR-CONICYT Grant No. 39, "Colors." M.G.C. acknowledges the financial support of FONDECYT Grant No. 1120320 and Anillo Grant No. ACT127. C.F.O. acknowledges the financial support of CONICYT by the Beca Magister Nacional and a program of the Ayuda de Estadías Cortas de Investigación of the University of Chile.

[1] G. Nicolis and I. Prigogine, *Self-Organization in Non Equilibrium Systems* (J. Wiley & Sons, New York, 1977).
[2] L. M. Pismen, *Patterns and Interfaces in Dissipative Dynamics*, Springer Series in Synergetics (Springer, Berlin, 2006).
[3] M. C. Cross and P. C. Hohenberg, Rev. Mod. Phys. **65**, 851 (1993).
[4] M. I. Rabinovich, A. B. Ezersky, and P. D. Weidman, *The Dynamics of Patterns* (World Scientific, Singapore, 2000).
[5] M. Cross and H. Greenside, *Pattern Formation and Dynamics in Nonequilibrium Systems* (Cambridge University Press, New York, 2009).
[6] P. Ball, *The Self-Made Tapestry: Pattern Formation in Nature* (Oxford University Press, New York, 1999).
[7] Y. Pomeau, Physica D **23**, 3 (1986).
[8] W. van Saarloos, Phys. Rep. **386**, 29 (2003).
[9] S. Residori, A. Petrossian, T. Nagaya, C. Riera, and M. G. Clerc, Physica D **199**, 149 (2004).
[10] P. Coullet, J. Lega, B. Houchmanzadeh, and J. Lajzerowicz, Phys. Rev. Lett. **65**, 1352 (1990); D. Michaelis, U. Peschel, F. Lederer, D. V. Skryabin, and W. J. Firth, Phys. Rev. E **63**, 066602 (2001); M. G. Clerc, S. Coulibaly, and D. Laroze, Int. J. Bifurcation Chaos Appl. Sci. Eng. **19**, 2717 (2009).
[11] D. Bensimon, B. I. Shraiman, and V. Croquette, Phys. Rev. A **38**, 5461 (1988).
[12] S. H. Strogatz, *Nonlinear Dynamics and Chaos* (Westview Press, Cambridge, MA, 2000).
[13] M. G. Clerc, R. G. Elias, and R. G. Rojas, Philos. Trans. R. Soc., A **369**, 412 (2011).
[14] F. Haudin, R. G. Elias, R. G. Rojas, U. Bortolozzo, M. G. Clerc, and S. Residori, Phys. Rev. Lett. **103**, 128003 (2009); Phys. Rev. E **81**, 056203 (2010).
[15] R. K. Dodd, J. C. Eilbeck, J. D. Gibbon, and H. C. Morris, *Solitons and Nonlinear Wave Equations* (Academic Press, London, 1982).
[16] M. Remoissenet, *Waves Called Solitons* (Springer, Berlin, 1996).
[17] P. Ramon, *Field Theory: A Modern Primer*, Frontiers in Physics Series, Vol. 74 (Westview Press, Boulder, CO, 1989).
[18] M. G. Clerc, S. Coulibaly, and D. Laroze, Int. J. Bifurcation Chaos Appl. Sci. Eng. **19**, 3525 (2009).
[19] E. I. Butikov, J. Phys. A **35**, 6209 (2002); Am. J. Phys. **69**, 755 (2001).
[20] P. Holmes, J. L. Lumley, and G. Berkooz, *Turbulence, Coherent Structures, Dynamical Systems and Symmetry* (Cambridge University Press, Cambridge, 1998).
[21] L. D. Landau and E. M. Lifshiftz, *Mechanics* (Pergamon, Oxford, 1976).
[22] A. Stephenson, Philos. Mag. Series 6 **15**, 233 (1908).
[23] M. G. Clerc, C. Falcon, C. Fernandez-Oto, and E. Tirapegui, Europhys. Lett. **98**, 30006 (2012).
[24] H. P. Kalmus, Am. J. Phys. **38**, 874 (1970); M. M. Michaelis, *ibid.* **53**, 1079 (1985); M. H. Friedman, J. E. Campana, and A. L. Yergey, *ibid.* **50**, 924 (1982).
[25] H. J. T. Smith and J. A. Blackburn, Am. J. Phys. **60**, 909 (1992).
[26] P. L. Kapitza, Sov. Phys. JETP **21**, 588 (1951) [in Russian]; see also *Collected Papers of P. L. Kapitza*, edited by D. Ter Haar (Pergamon, London, 1965), p. 714.
[27] R. E. Goldstein, G. H. Gunaratne, L. Gil, and P. Coullet, Phys. Rev. A **43**, 6700 (1991).
[28] P. M. Morse and H. Feshbach, *Methods of Theoretical Physics* (MacGraw-Hill, New York, 1953).
[29] C. M. Bender and S. A. Orzag, *Advanced Mathematical Methods for Scientists and Engineers* (McGraw-Hill, New York, 1978).
[30] R. Gilmore, *Catastrophe Theory, for Scientists and Engineers* (John Wiley and Sons, New York, 1981).
[31] J. Boa and D. S. Cohen, SIAM J. Appl. Math. **30**, 123 (1976).
[32] N. Akhmediev and A. Ankiewicz, *Dissipative Solitons*, Lecture Notes in Physics (Springer, Berlin, 2005).
[33] *Localized States in Physics: Solitons and Patterns*, edited by O. Descalzi, M. Clerc, S. Residori, and G. Assanto (Springer, Berlin, 2011).
[34] H. G. Purwins, H. U. Bodeker, and Sh. Amiranashvili, Adv. Phys. **59**, 485 (2010).
[35] T. Ackemann, W. J. Firth, and G. L. Oppo, in *Fundamentals and Applications of Spatial Dissipative Solitons in Photonic Devices*, edited by E. Arimondo, P. R. Berman, and C. C. Lin, special issue of Adv. At., Mol., Opt. Phys. **57**, 323 (2009).
[36] P. Coullet, Int. J. Bifurcation Chaos **12**, 2445 (2002).
[37] H. Sakaguchi and H. Brand, Physica D **97**, 274 (1996).
[38] S. Fauve and O. Thual, Phys. Rev. Lett. **64**, 282 (1990); O. Thual and S. Fauve, J. Phys. (France) **49**, 1829 (1988).
[39] S. Barland, J. R. Tredicce, M. Brambilla, L. A. Lugiato, S. Balle, M. Giudici, T. Maggipinto, L. Spinelli, G. Tissoni, T. Knodlk, M. Millerk, and R. Jagerk, Nature (London) **419**, 699 (2002).
[40] P. Coullet, C. Riera, and C. Tresser, Phys. Rev. Lett. **84**, 3069 (2000).
[41] W. van Saarloos and P. C. Hohenberg, Phys. Rev. Lett. **64**, 749 (1990).

[42] P. D. Woods and A. R. Champneys, Physica D **129**, 147 (1999).
[43] G. W. Hunt, G. J. Lord, and A. R. Champneys, Comput. Methods Appl. Mech. Eng. **170**, 239 (1999).
[44] J. Burke and E. Knobloch, Phys. Rev. E **73**, 056211 (2006).
[45] J. Burke and E. Knobloch, Chaos **17**, 037102 (2007).
[46] M. G. Clerc and C. Falcon, Physica A **356**, 48 (2005).
[47] U. Bortolozzo, M. G. Clerc, C. Falcon, S. Residori, and R. Rojas, Phys. Rev. Lett. **96**, 214501 (2006).
[48] F. Haudin, R. G. Rojas, U. Bortolozzo, S. Residori, and M. G. Clerc, Phys. Rev. Lett. **107**, 264101 (2011).